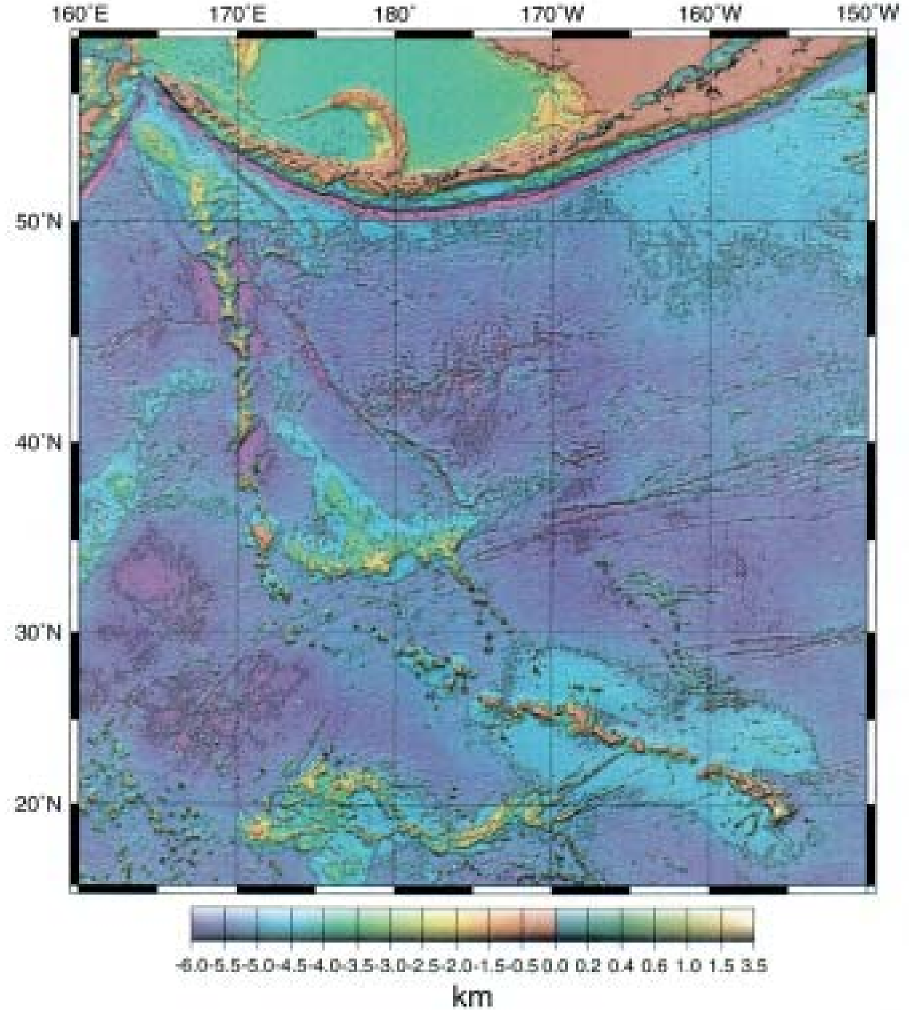

Figure 11.2. (a) Seafloor topography in the region around the Hawaiian-Emperor chain, after Smith and Sandwell (1997).

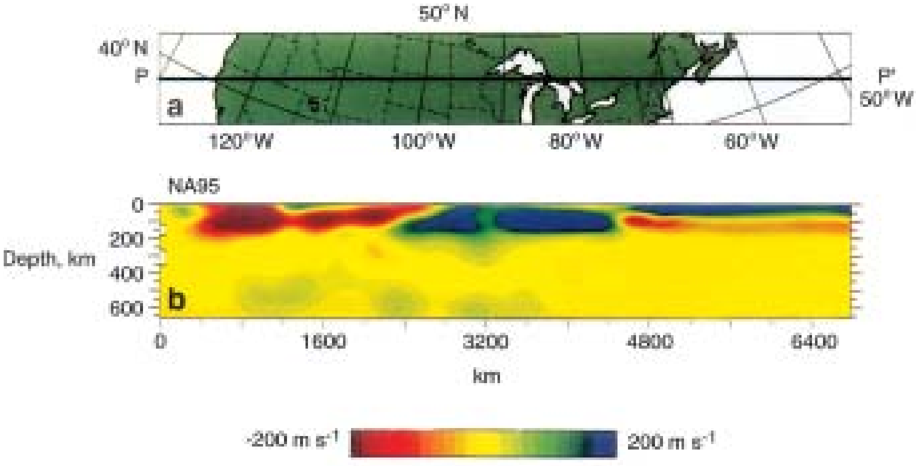

Figure 11.8. Cross-section of upper mantle seismic shear wave velocity variations beneath North America along PP′, determined by van der Lee and Nolet (1997).

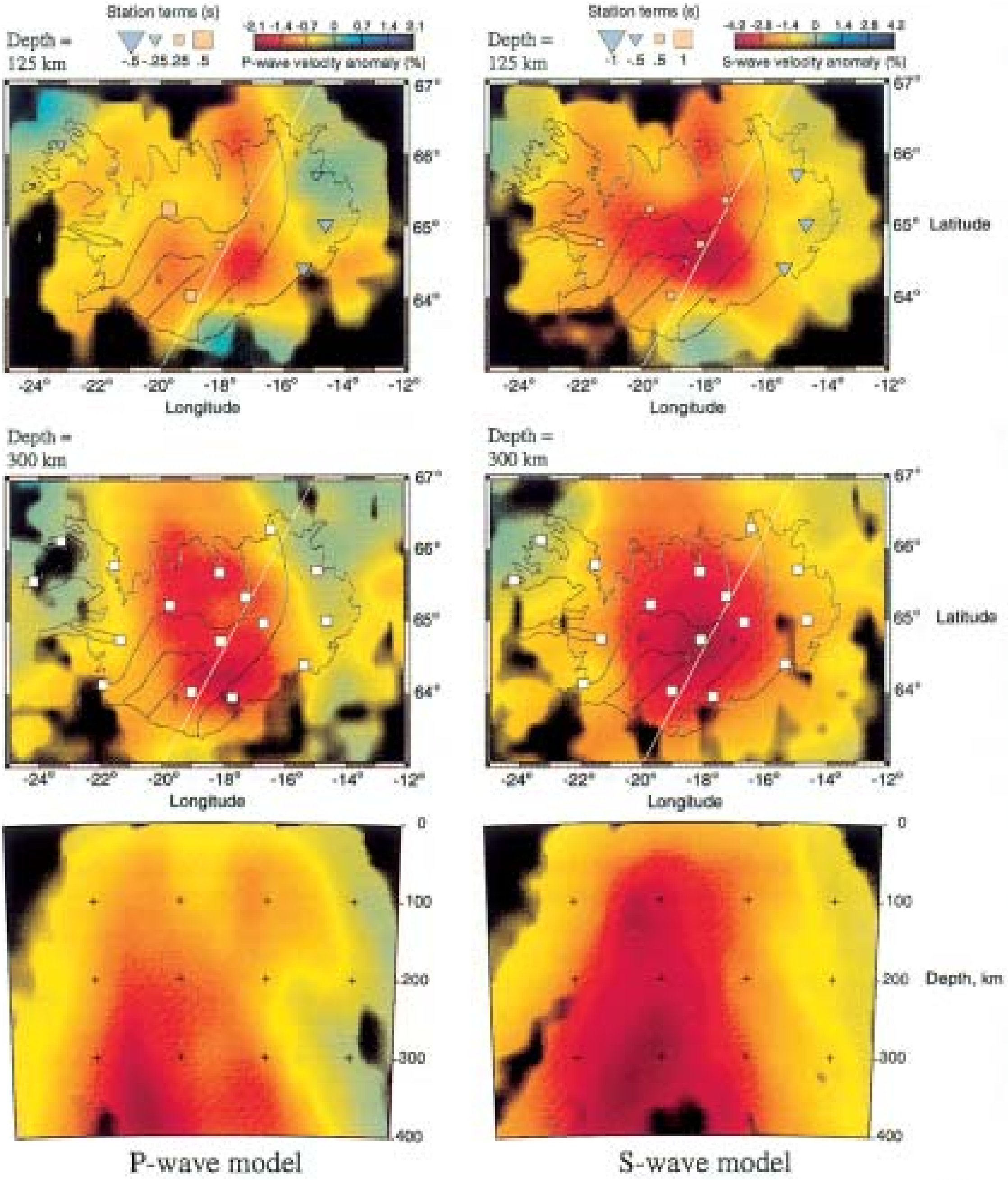

Figure 11.9. Upper mantle compressional wave velocity (left) and shear wave velocity (right) variations beneath Iceland determined by Wolfe et al. (1997). Variations at 125 km depth (top row), 300 km depth (middle row), and in cross-section (bottom row).

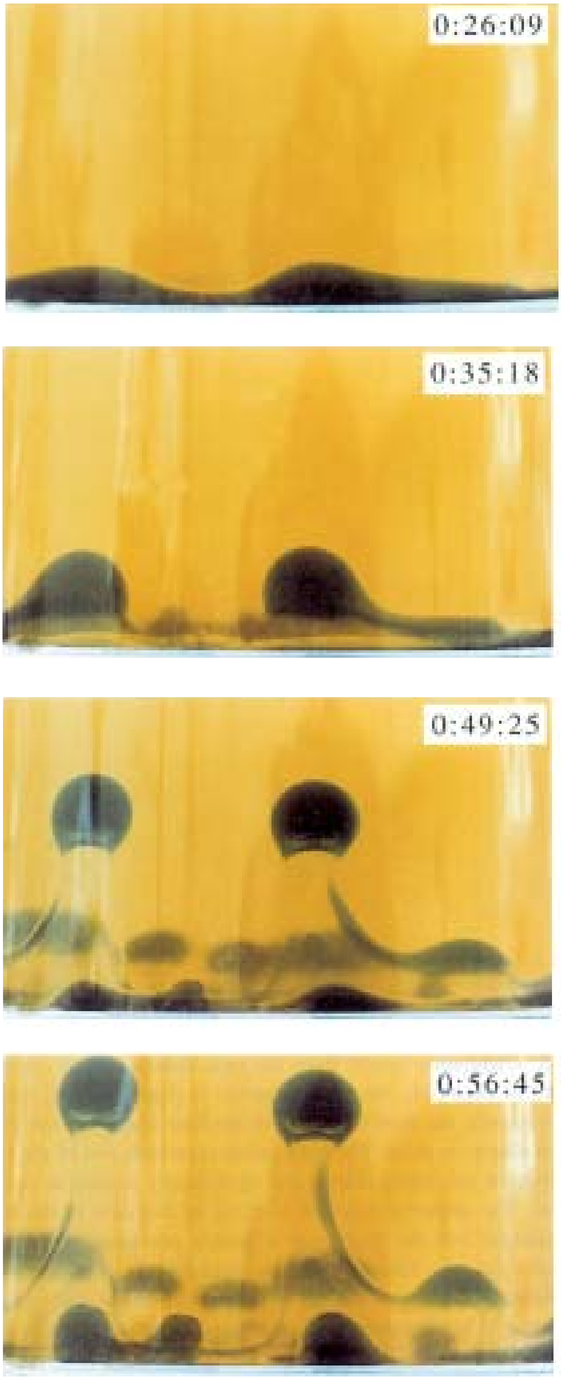

Figure 11.11. Photographs from a laboratory experiment showing plume initiation by instability of a thin, low-density, low-viscosity glucose fluid layer beneath a deep, high-density, high-viscosity glucose fluid layer. Times and depth scale are indicated. From Bercovici and Kelly (1997).

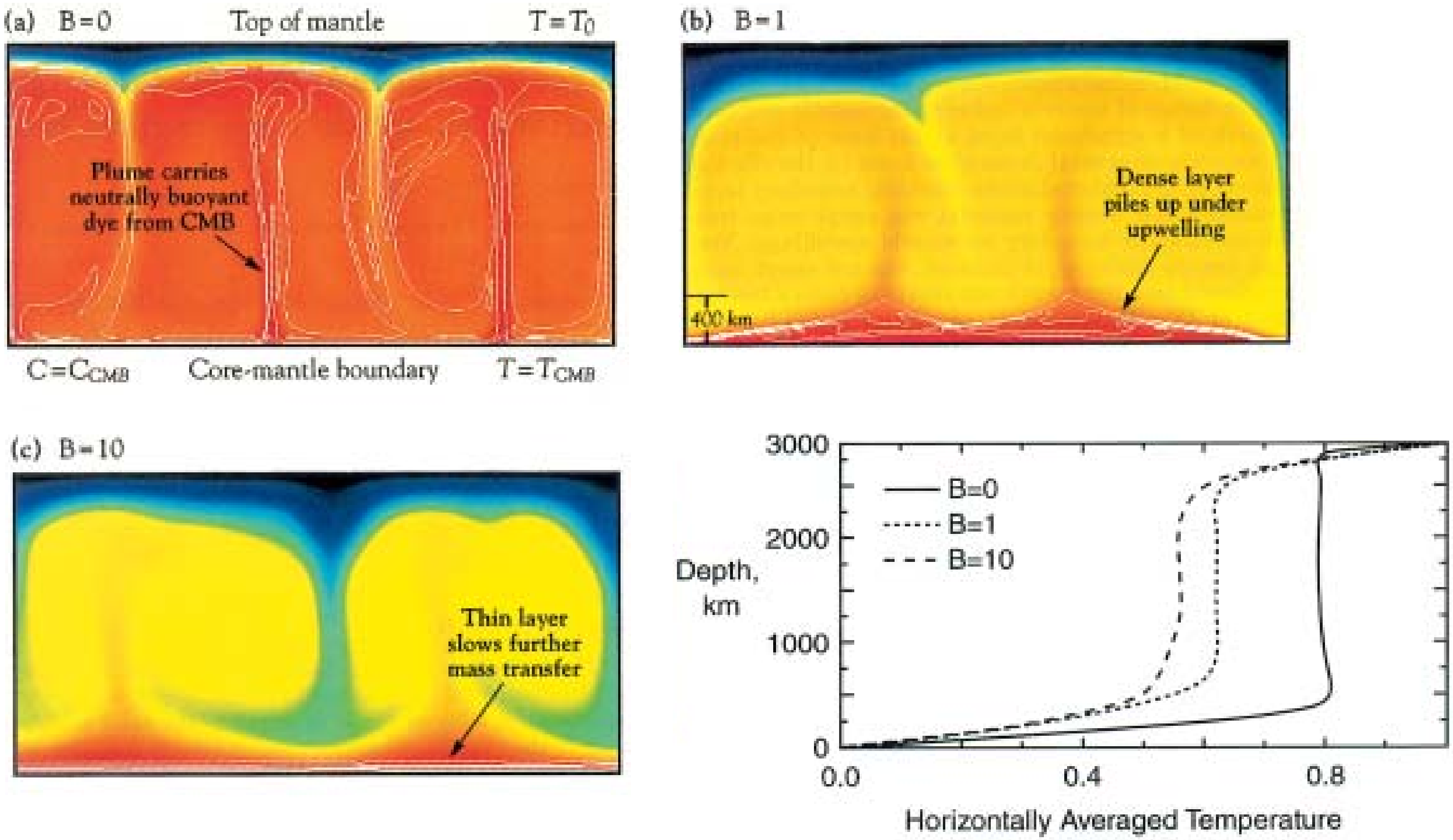

Figure 11.12. (a–c) Variation of temperature (shades) and composition (contours) in two-dimensional numerical calculations by Kellogg (1997) of thermochemical convection in the D″ layer for different values of *B*, the ratio of compositional to thermal buoyancy. (d) Laterally averaged temperature profiles for cases a–c.

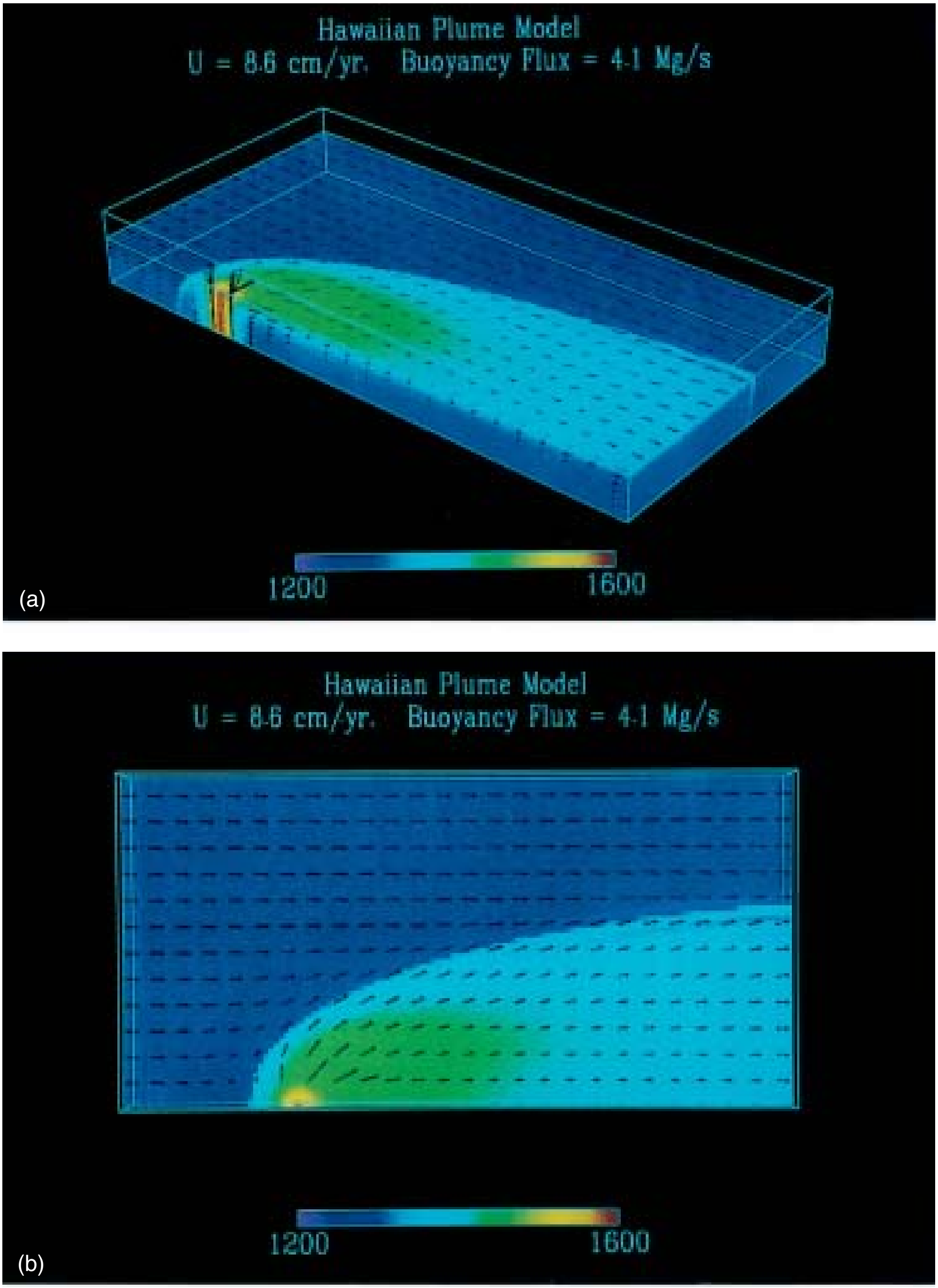

Figure 11.22. Results of a three-dimensional numerical calculation of a thermal plume beneath a moving plate, from Ribe and Christensen (1994). Arrows show fluid velocity; contours are temperatures in degree Celsius. Parameters are chosen for the Hawaiian hot spot. (a) Oblique side view; (b) top view. The surface displayed in (b) is at 150 km depth.

Figure 14.4. Global view of the surface of Venus centered at 180° east longitude based on Magellan synthetic aperture radar mosaics and Pioneer Venus Orbiter data.

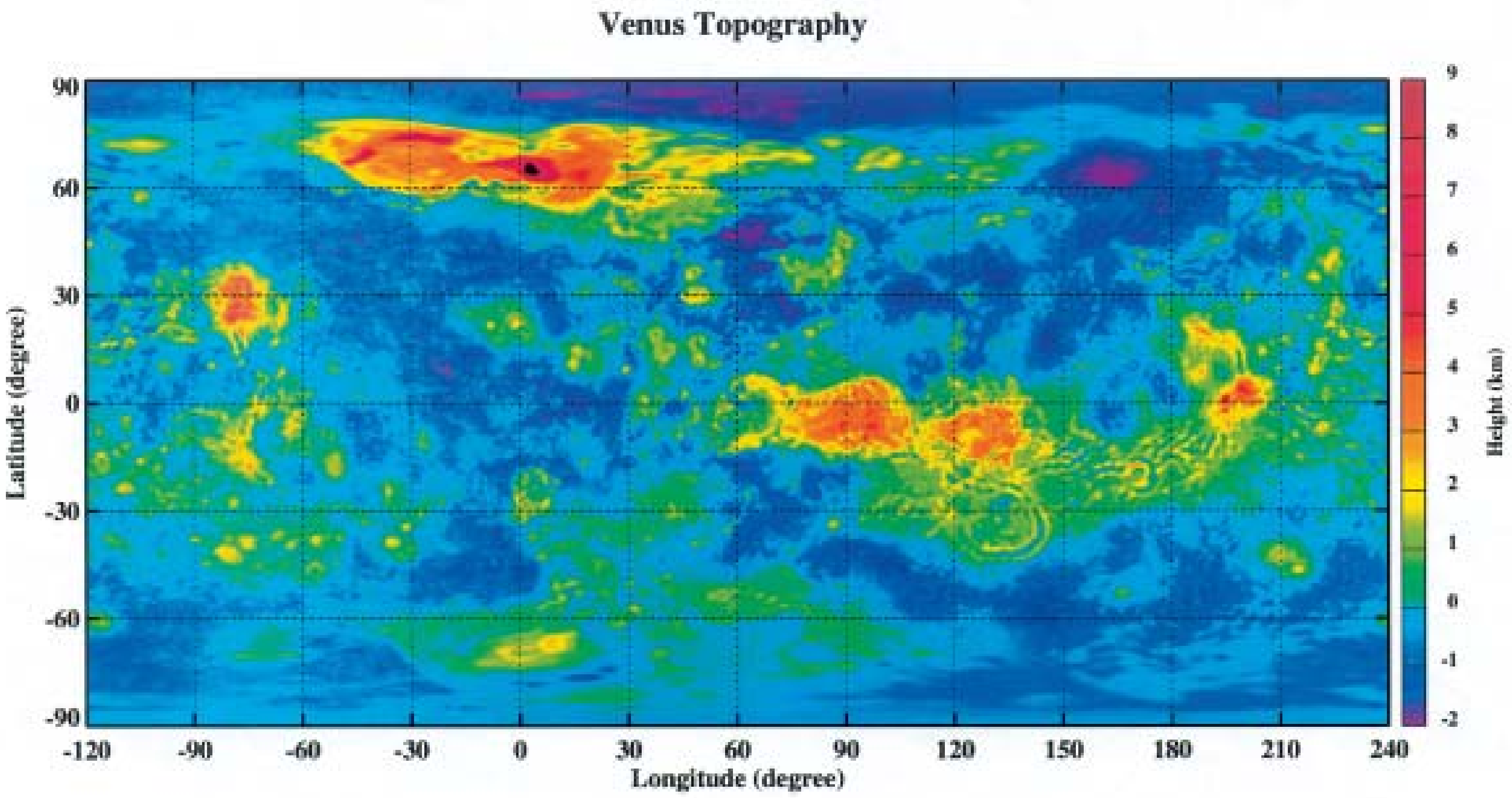

Figure 14.5. Venus topography from a 360 degree and order spherical harmonic model (Rappaport et al., 1999). The plot is based on a truncation of the model to degree and order 180.

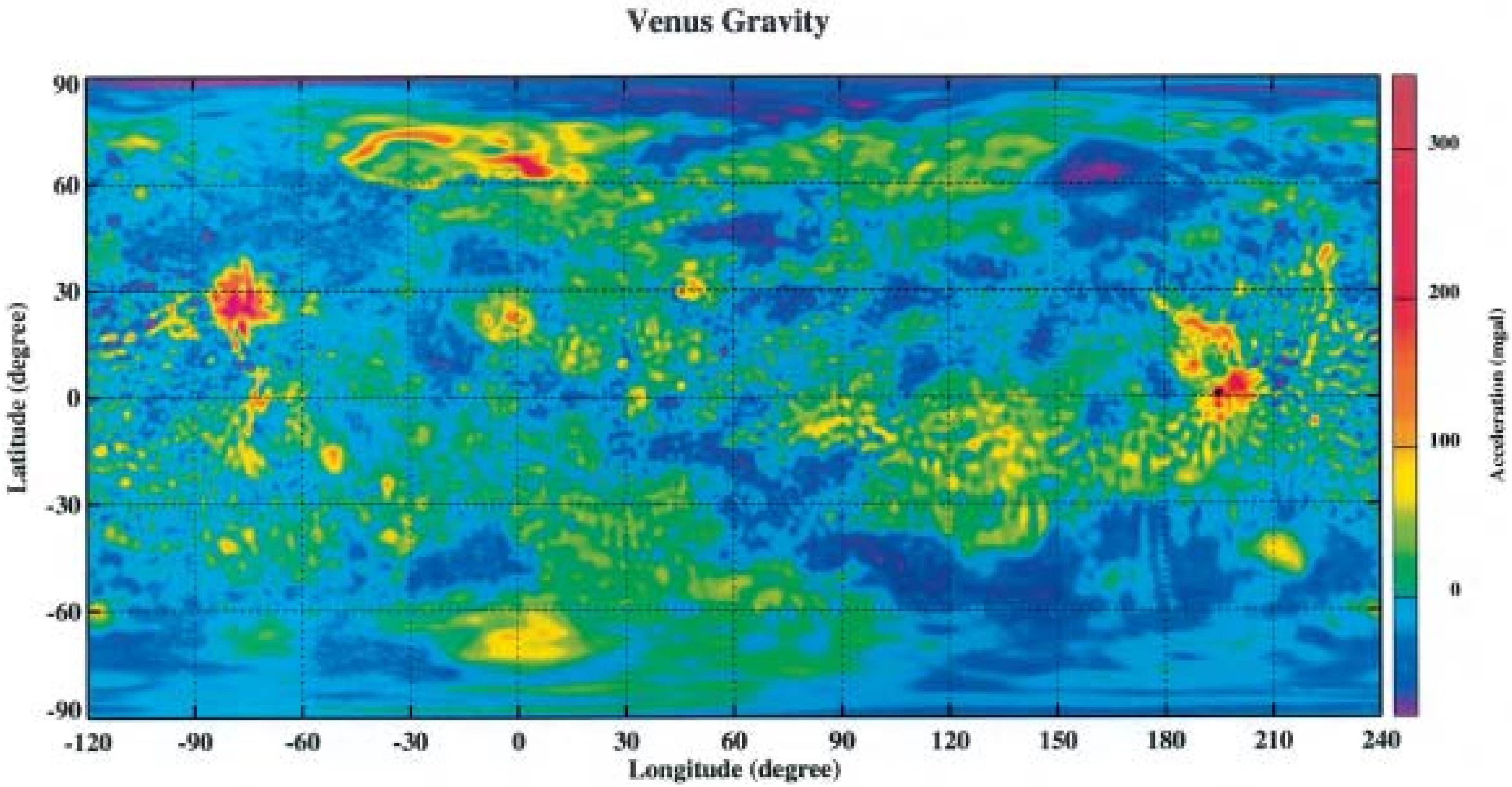

Figure 14.6. Venus gravity field from a 180 degree and order spherical harmonic model (Konopliv et al., 1999). The plot is based on a truncation of the model to degree and order 150.

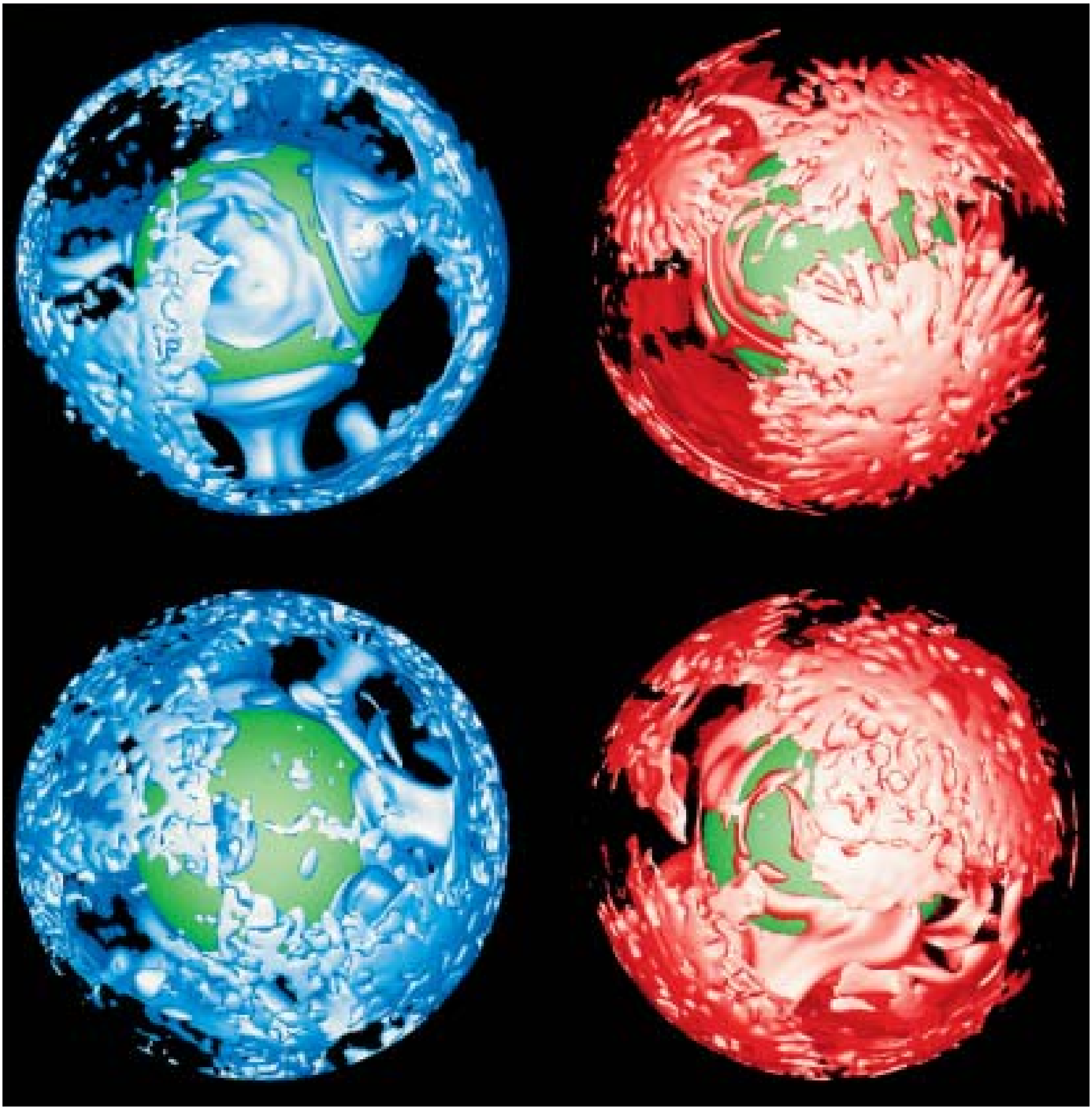

Figure 14.11. Cold downwellings (left) and hot upwellings (right) in the two spherical convection models of Venusian mantle convection. Illustrated are isosurfaces of residual temperature (temperature difference from the horizontally averaged geotherm), showing where the temperature is 110 K lower (left) or 110 K higher (right) than the geotherm. The upper plots show case 1, with the rigid upper surface; the lower plots show case 2, with the free-slip upper surface. Convection in these models is time dependent; the time step shown is typical of the convective state. After Schubert et al. (1997).

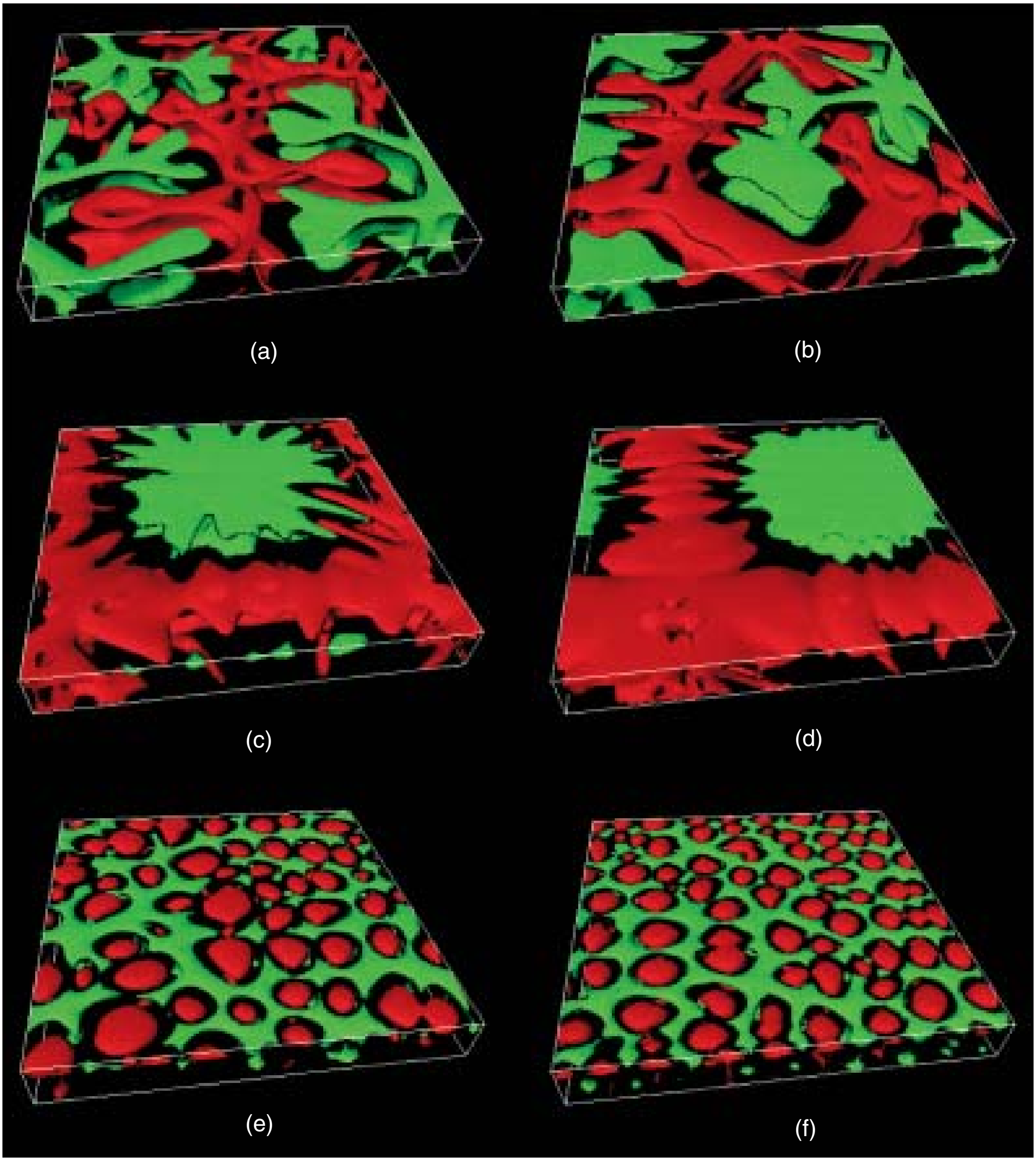

Figure 14.15. A series of Boussinesq calculations in an $8 \times 8 \times 1$ Cartesian box with fixed Rayleigh number based on the viscosity at the mean of the top and bottom boundary temperatures of 10^5 and increasing viscosity contrast. Figures show isosurfaces of residual temperature ΔT, i.e., temperature relative to a horizontally averaged temperature profile, with green (dark) surfaces representing cold (downwelling) material and red (light) surfaces representing hot (upwelling) material. (a) Constant viscosity, surfaces show $\Delta T = \pm 0.1$; (b) $\Delta\eta = 10$, $\Delta T = \pm 0.1$; (c) $\Delta\eta = 100$, $\Delta T = \pm 0.1$; (d) $\Delta\eta = 1000$, $\Delta T = \pm 0.1$; (e) $\Delta\eta = 10^4$, $\Delta T = \pm 0.075$; and (f) $\Delta\eta = 10^5$, $\Delta T = \pm 0.05$.

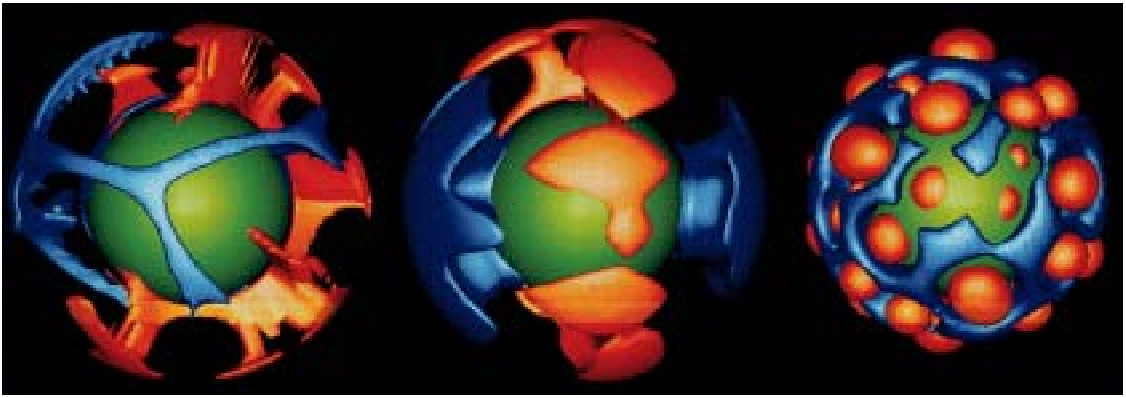

Figure 14.16. Similar to Figure 14.15 but for convection in a spherical shell with a ratio of inner radius to outer radius of 0.55. The viscosity contrasts, from left to right, are 1, 10^3, and 10^4. The residual temperature surfaces, from left to right, are (+0.2, −0.15), (+0.2, −0.15), and ±0.15. Blue surfaces represent cold (downwelling) material and red or orange surfaces represent hot (upwelling) material. The green sphere represents the inner boundary of the model.

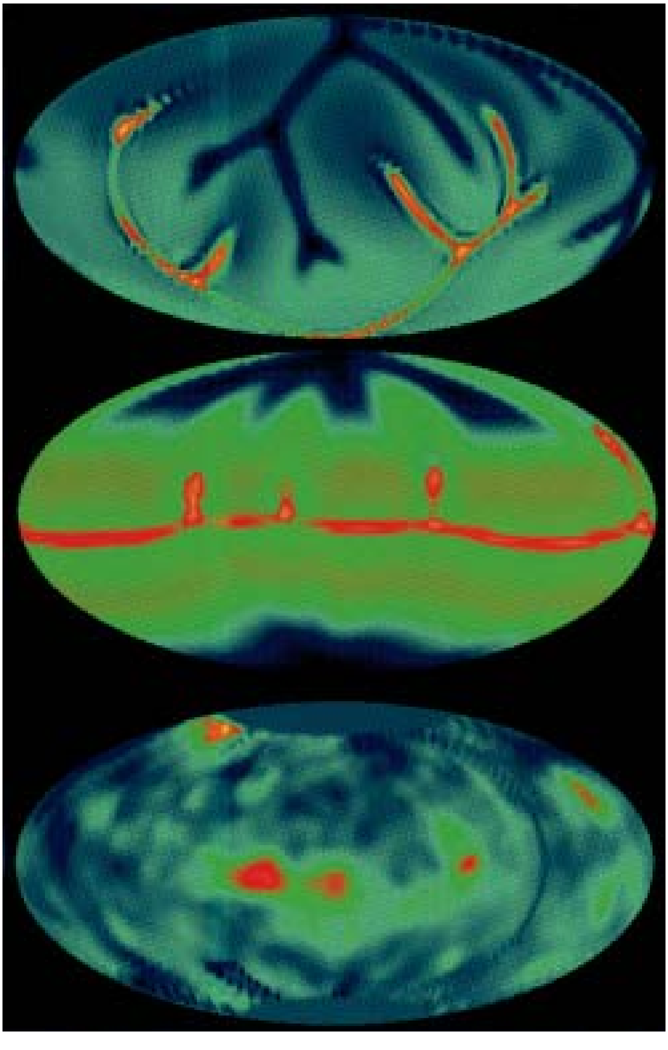

Figure 14.18. Patterns of convection in a spherical shell for constant viscosity (top), variable viscosity with a viscosity contrast of 10^3 (middle), and the topography of Venus (bottom). The convection patterns are illustrated by the temperature variations at mid-depth. Blue (dark) indicates either cold (downwelling) fluid or low topography. Red (light) indicates either hot (upwelling) fluid or high topography. The temperature fields and topography are displayed on a Hammer-Aitoff equal-area projection (after Ratcliff et al., 1995).

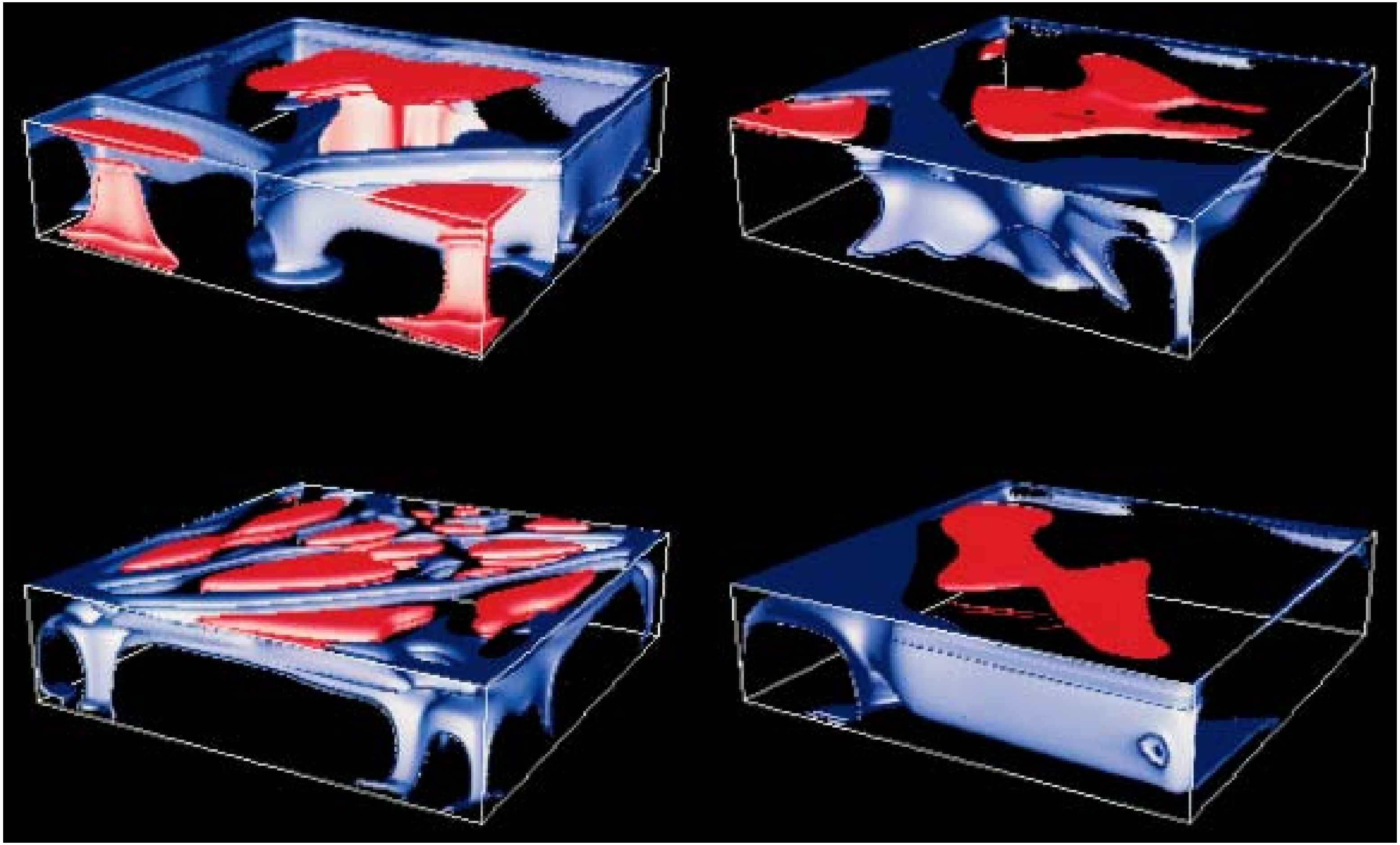

Figure 14.19. Cold downwellings (blue) and hot upwellings (red) for the three variable viscosity phase change cases. Plotted are isosurfaces of residual temperature, i.e., temperature relative to the horizontally averaged temperature profile, showing where the temperature is ±0.1 from the horizontal average. (a) (Top left) constant viscosity case 1, (b) (lower left) variable viscosity case 2, (c) and (d) (right) variable viscosity with a yield stress (case 3) at two different times.

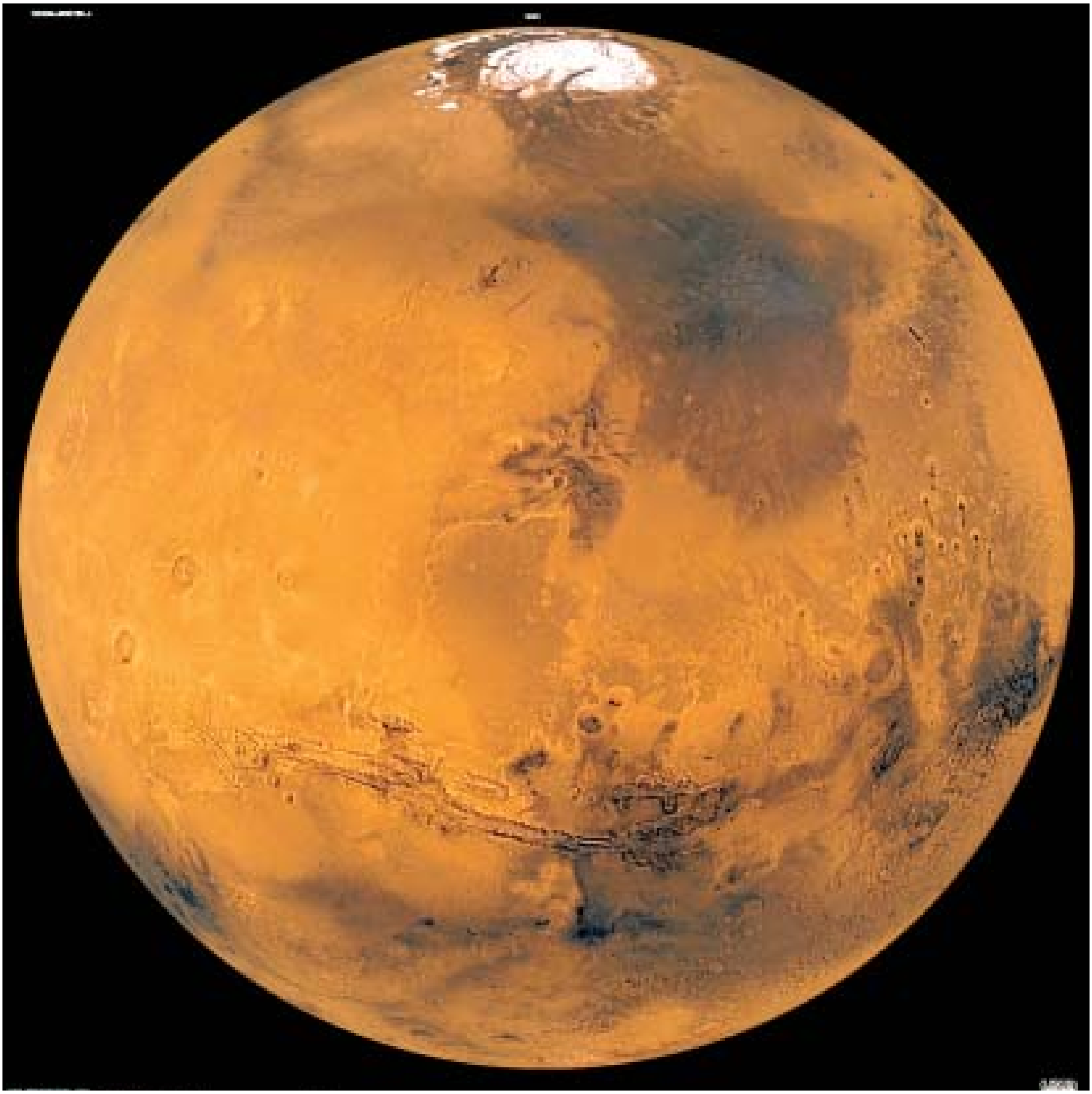

Figure 14.27. View of Mars from Viking Orbiter mosaics. The orthographic view is centered at 20° latitude and 60° longitude. The north polar cap is visible at the top of the image, the equatorial canyon system Valles Marineris is below the center, and the four Tharsis volcanoes are at the left. The view shows the heavily cratered southern hemisphere highlands and the younger, less heavily cratered terrains in the northern hemisphere.

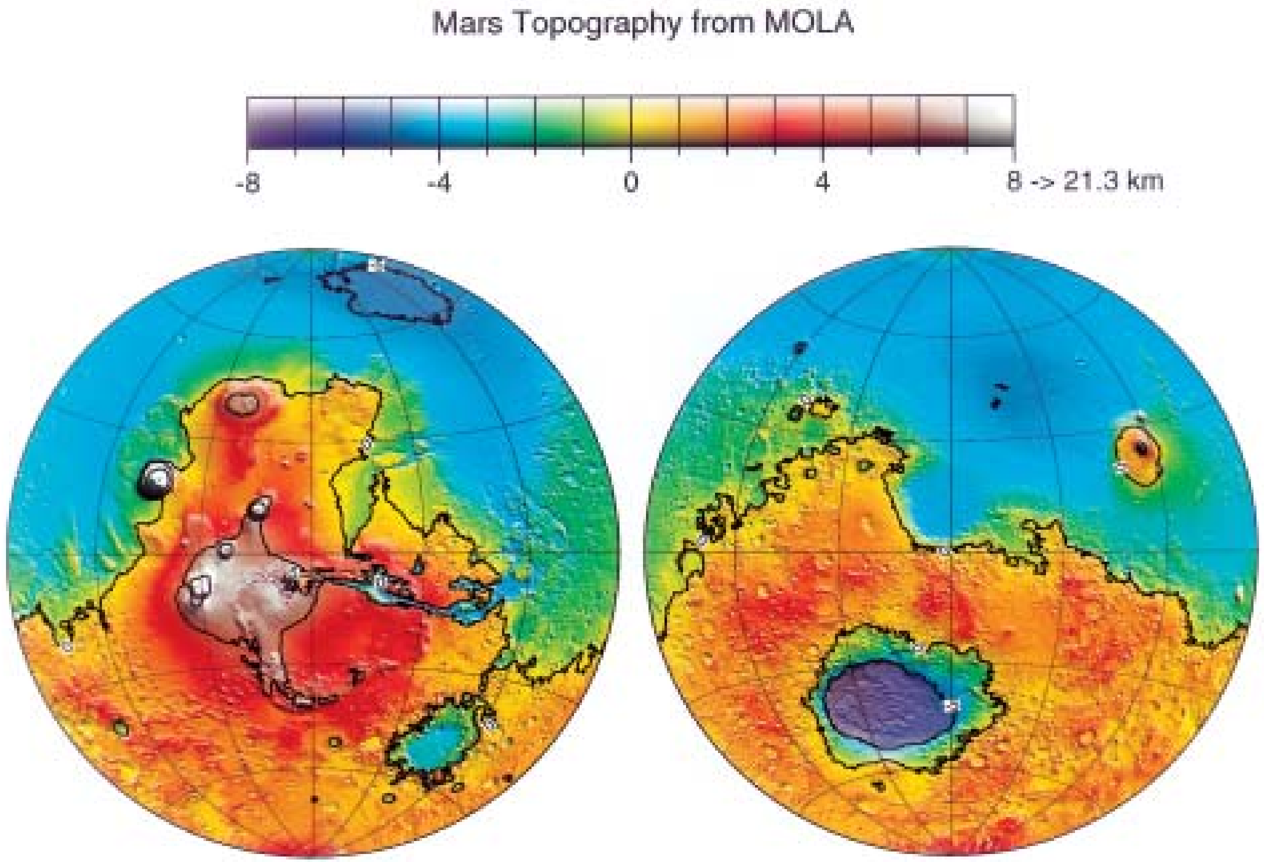

Figure 14.28. A 1° × 1° global map of the topography of Mars from the Mars Orbiter Laser Altimeter (MOLA) on the Mars Global Surveyor spacecraft. One degree corresponds to 59 km at the equator. The global accuracy of the map is 13 m. The zero level of topography is the average radius (3,396.0 km) of the equatorial aeroid. Based on data reported in Smith et al. (1999a).

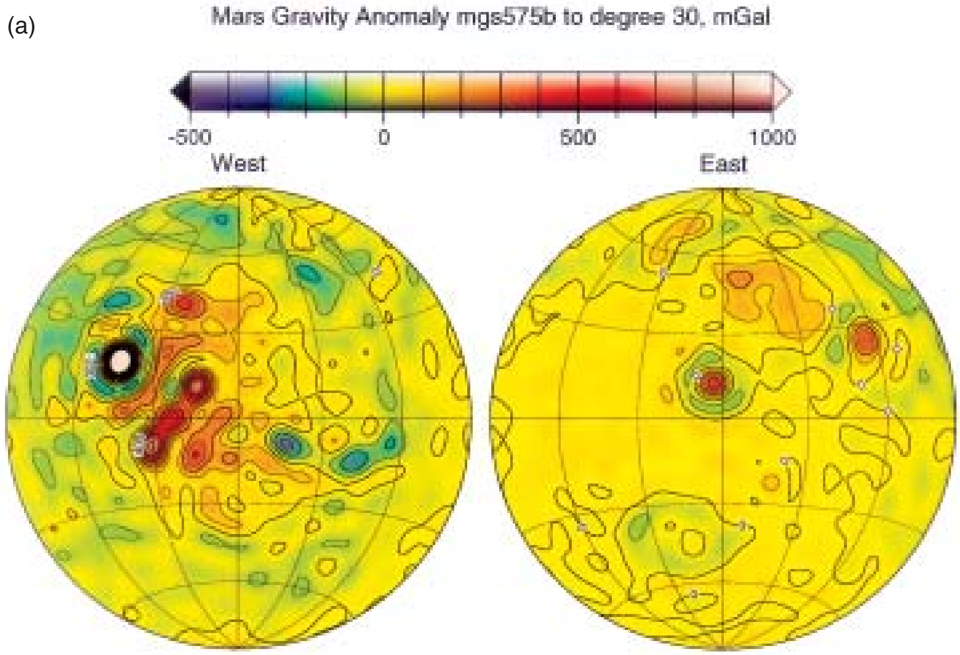

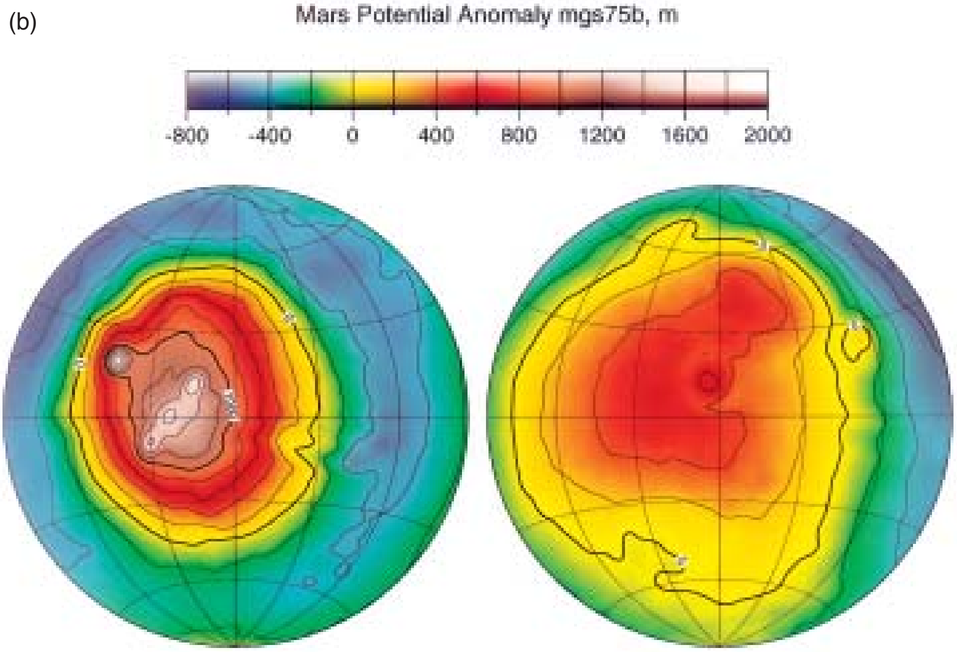

Figure 14.29. (a) Free-air gravity map of Mars from a 30th degree and order spherical harmonic representation of Mars Global Surveyor Doppler tracking data (Smith et al., 1999b). The spatial resolution is about 350 km. The gravity field has 95% of J_2 removed since 5% of J_2 is assumed to be nonhydrostatic in origin. (b) Aeroid of Mars from the spherical harmonic representation of the gravitational field described in (a).

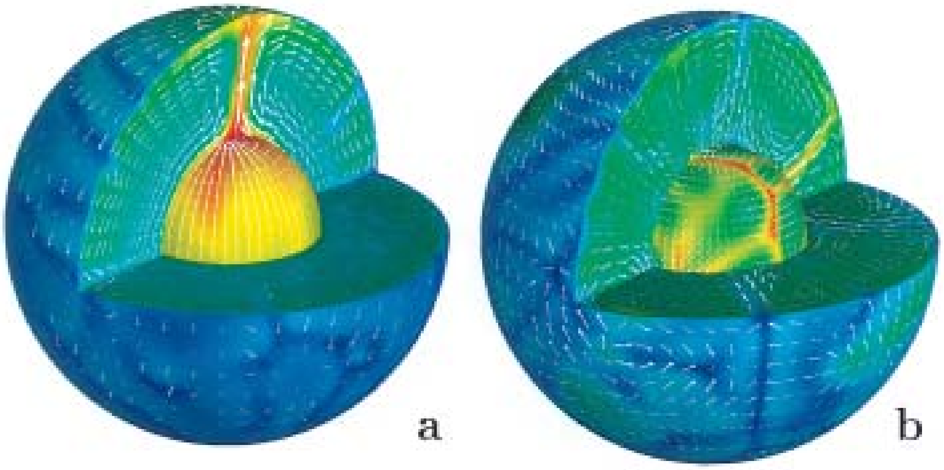

Figure 14.49. Cutaway views of the temperature and velocity field in a Martian mantle convection model with (a) and without (b) an endothermic phase change near the base of the model. The model is similar to the one described in Figure 14.48 except for the phase change which is only a nondimensional height of 0.04 (80 km) above the core–mantle boundary. In addition, the internal heating Rayleigh number is 6.5×10^6 and the basal heating Rayleigh number is 10^6. Only one plume dominates the mantle flow when the phase change is present. After Harder (1998).

Figure 14.50. View of the lunar surface obtained by the Galileo spacecraft in 1992 on its way to the Jovian system. The distinct bright ray crater at the bottom of the image is the Tycho impact basin. The dark areas are basalt-covered regions Oceanus Procellarum (on the left) and basalt-filled impact basins, Mare Imbrium (center left), Mare Serenitatis and Mare Tranquillitatis (center), and Mare Crisium (near the right edge).

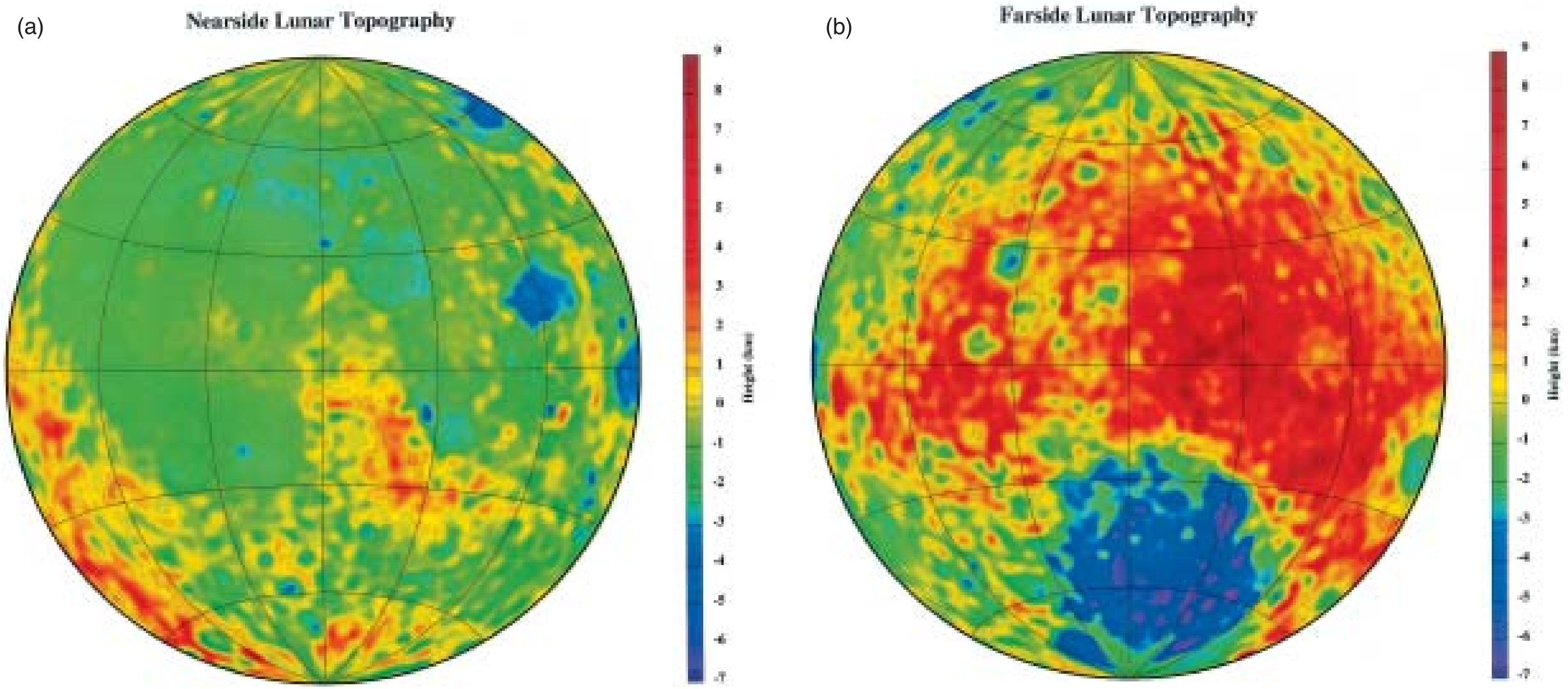

Figure 14.51. Topography of the lunar surface from Clementine lidar data (Smith et al., 1997). Nearside hemisphere (a), farside hemisphere (b). Topographic heights are with respect to a sphere of radius 1,737.1 km, the mean lunar radius. The large region of low-lying topography on the farside is the South Pole-Aitken basin. The topography is based on a spherical harmonic representation to degree and order 90.

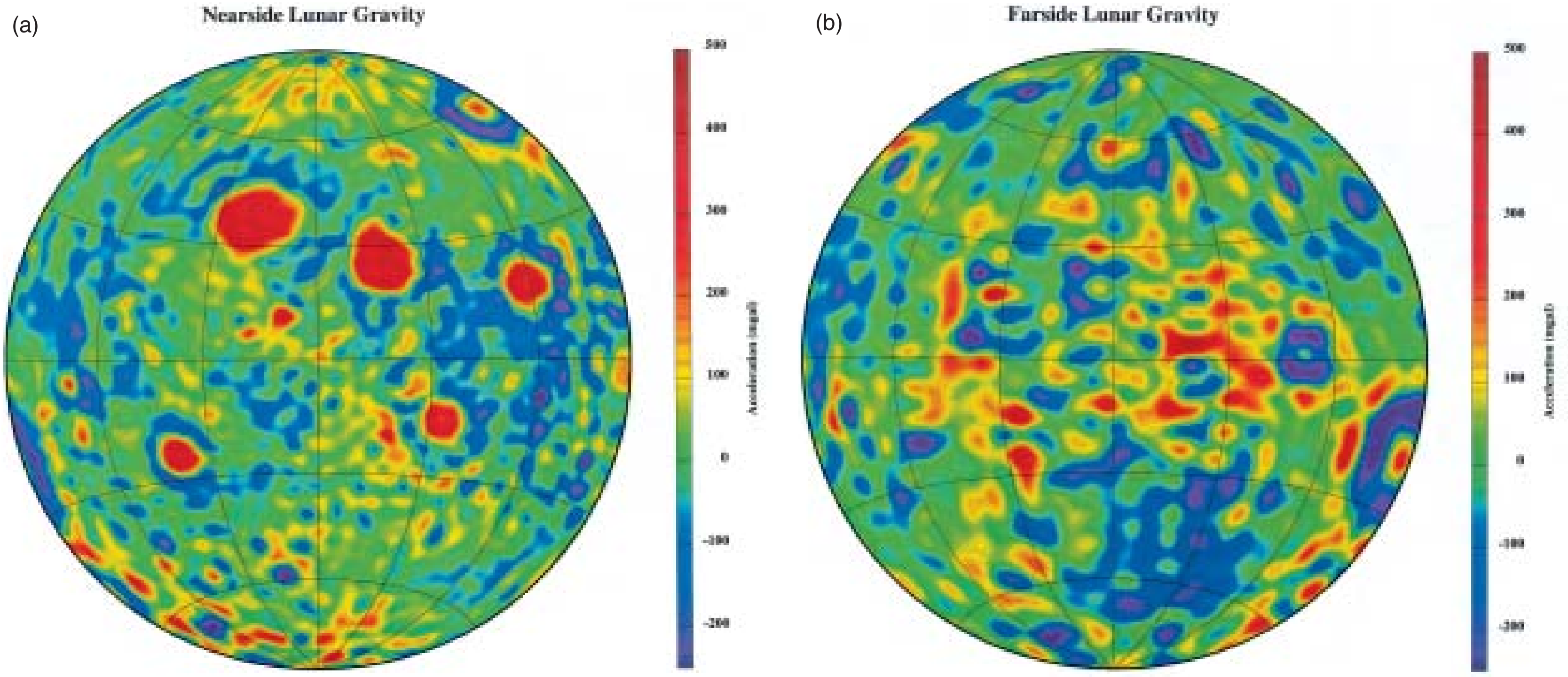

Figure 14.52. Gravity anomalies on the Moon. Lunar nearside (a), lunar farside (b). The gravity field is based on a spherical harmonic model of Lunar Prospector and other data to degree and order 100. After Konopliv and Yuan (1999).

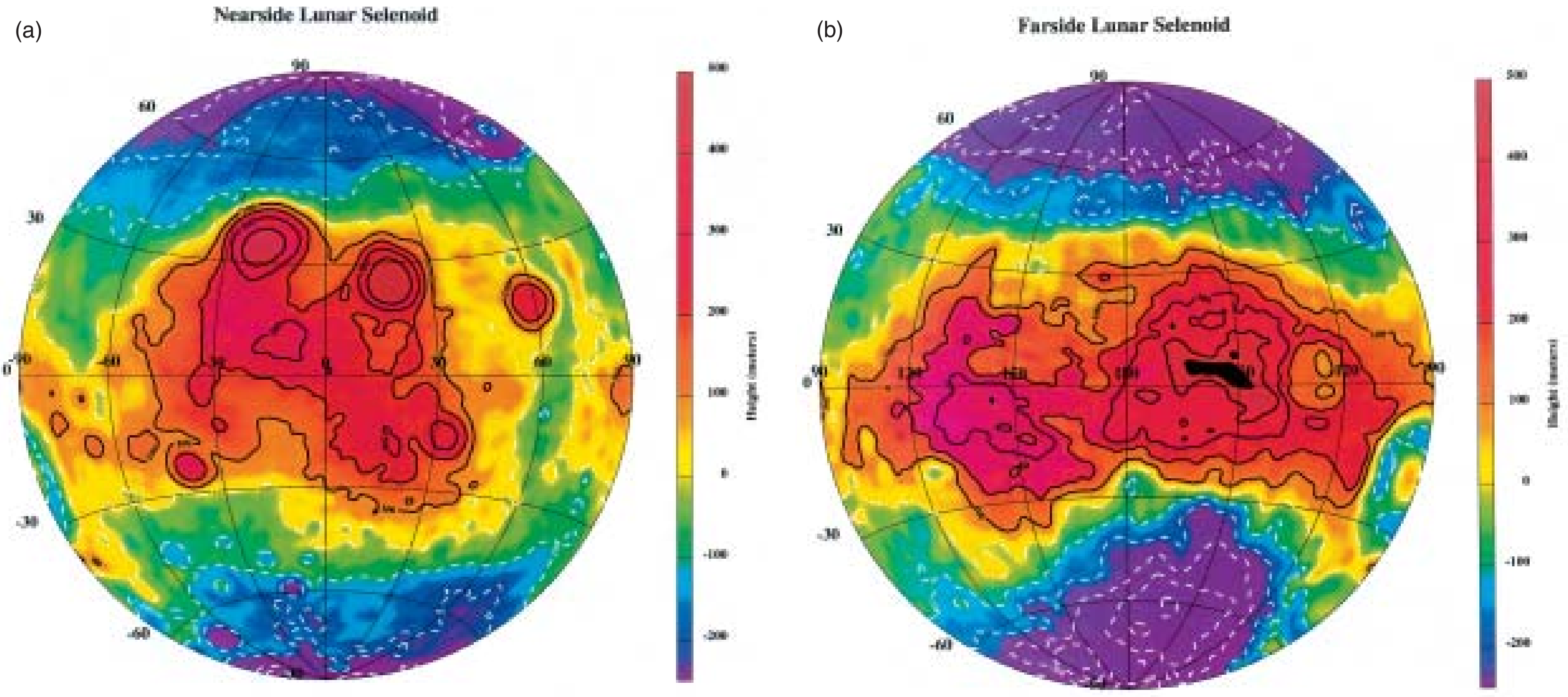

Figure 14.53. The lunar geoid or selenoid based on the gravity field in Figure 14.52. Nearside of the Moon (a) and farside (b). Selenoid heights are with respect to a reference radius of 1,738 km. After Konopliv and Yuan (1999).

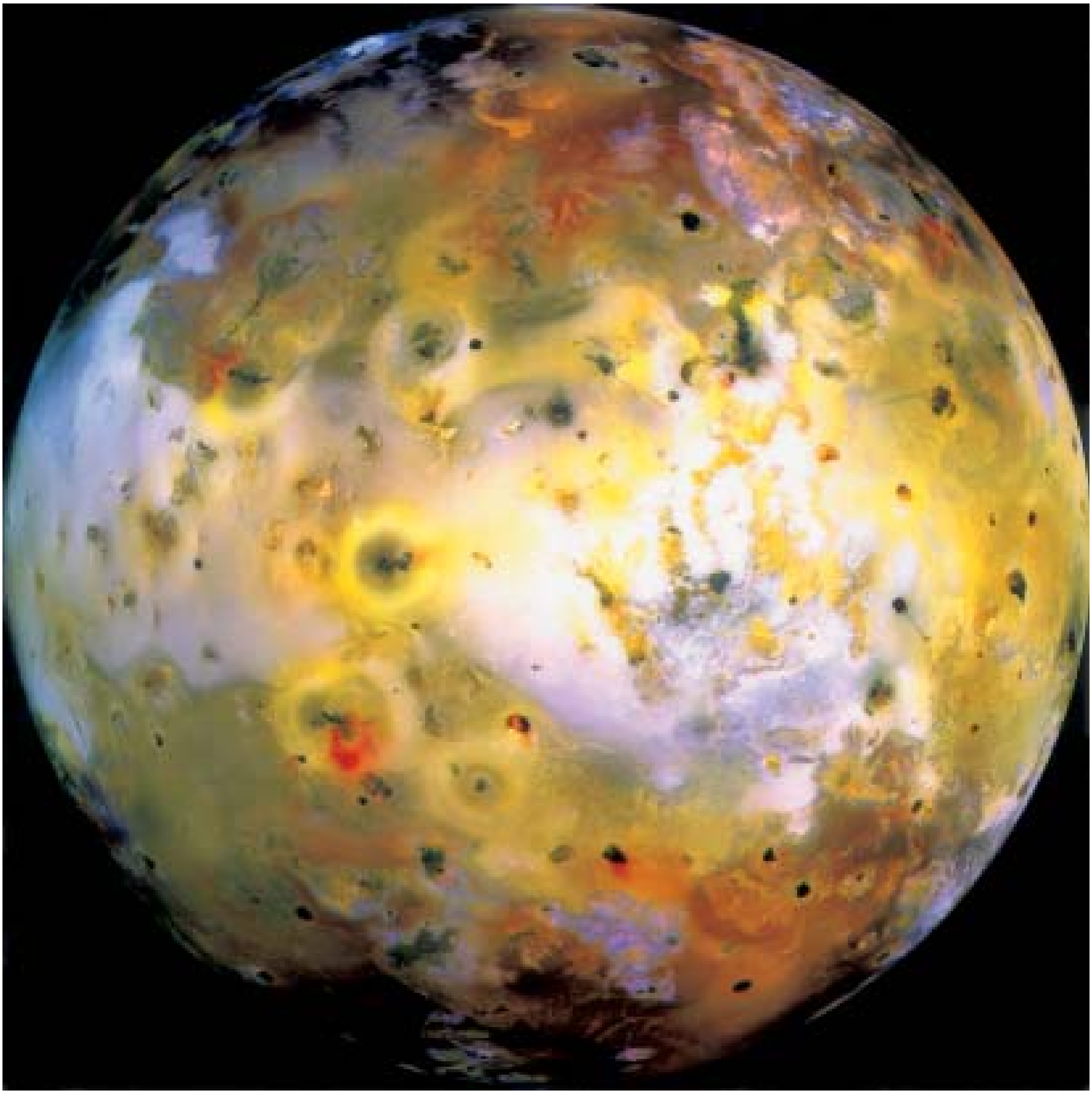

Figure 14.65. Global view of Jupiter's satellite Io from high-resolution (1.3 km per pixel) images obtained by the Galileo spacecraft on 3 July 1999. This false color mosaic uses near-infrared, green, and violet filters of the spacecraft's camera to enhance more subtle color variations. Surface features include mountains several kilometers high, layered materials forming plateaus, and irregular depressions or volcanic calderas. Some volcanic centers have bright, colorful flows possibly due to lavas with predominantly sulfur composition. Dark flow-like features may be silicate lava flows. Volcanic resurfacing has erased any evidence of impact craters. The picture is centered at 0.3° north latitude and 137.5° west longitude. North is to the top of the picture and the sun illuminates the surface from almost directly behind the spacecraft.

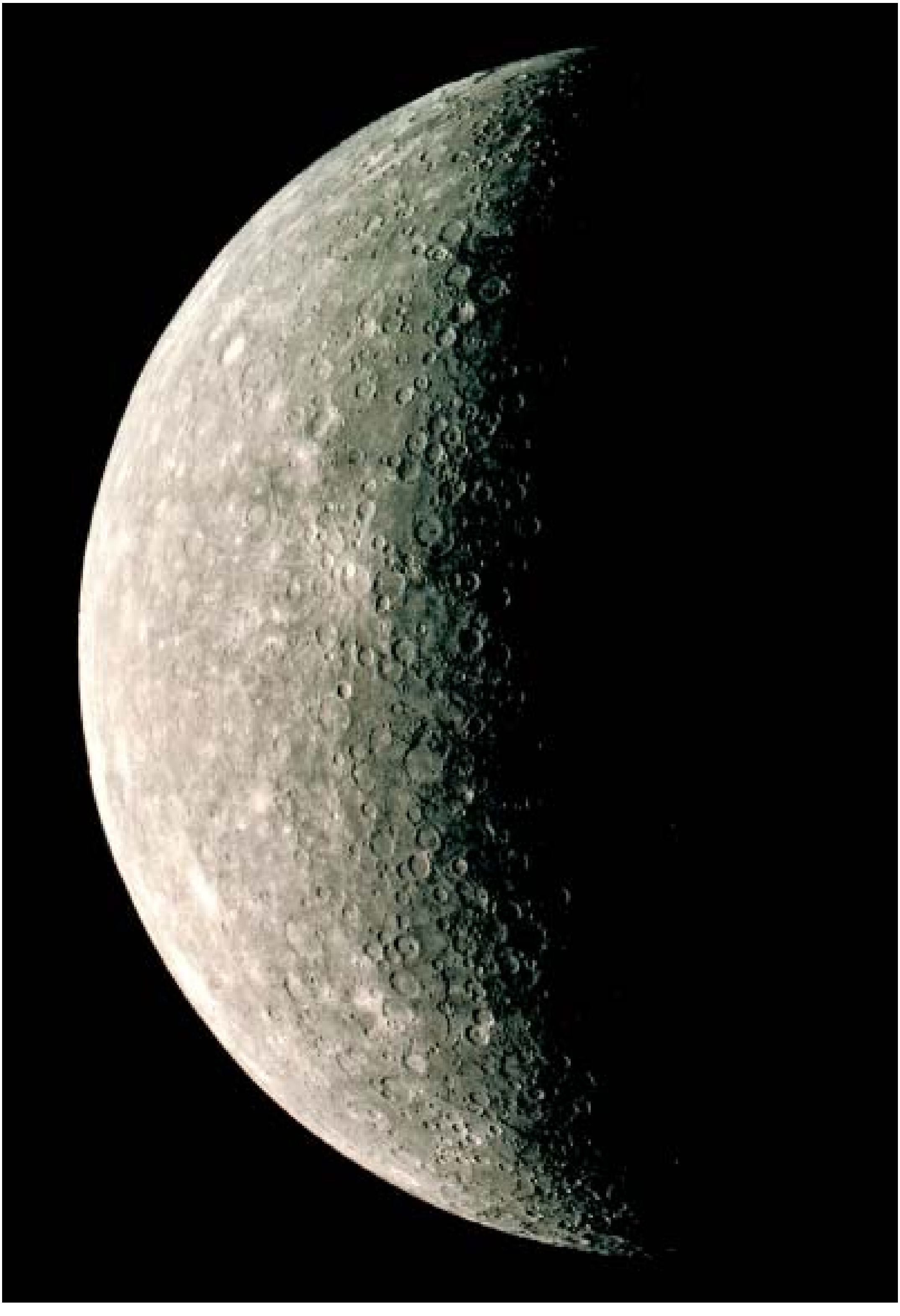

Figure 14.70. Mariner 10 image of Mercury acquired on 24 March 1974.

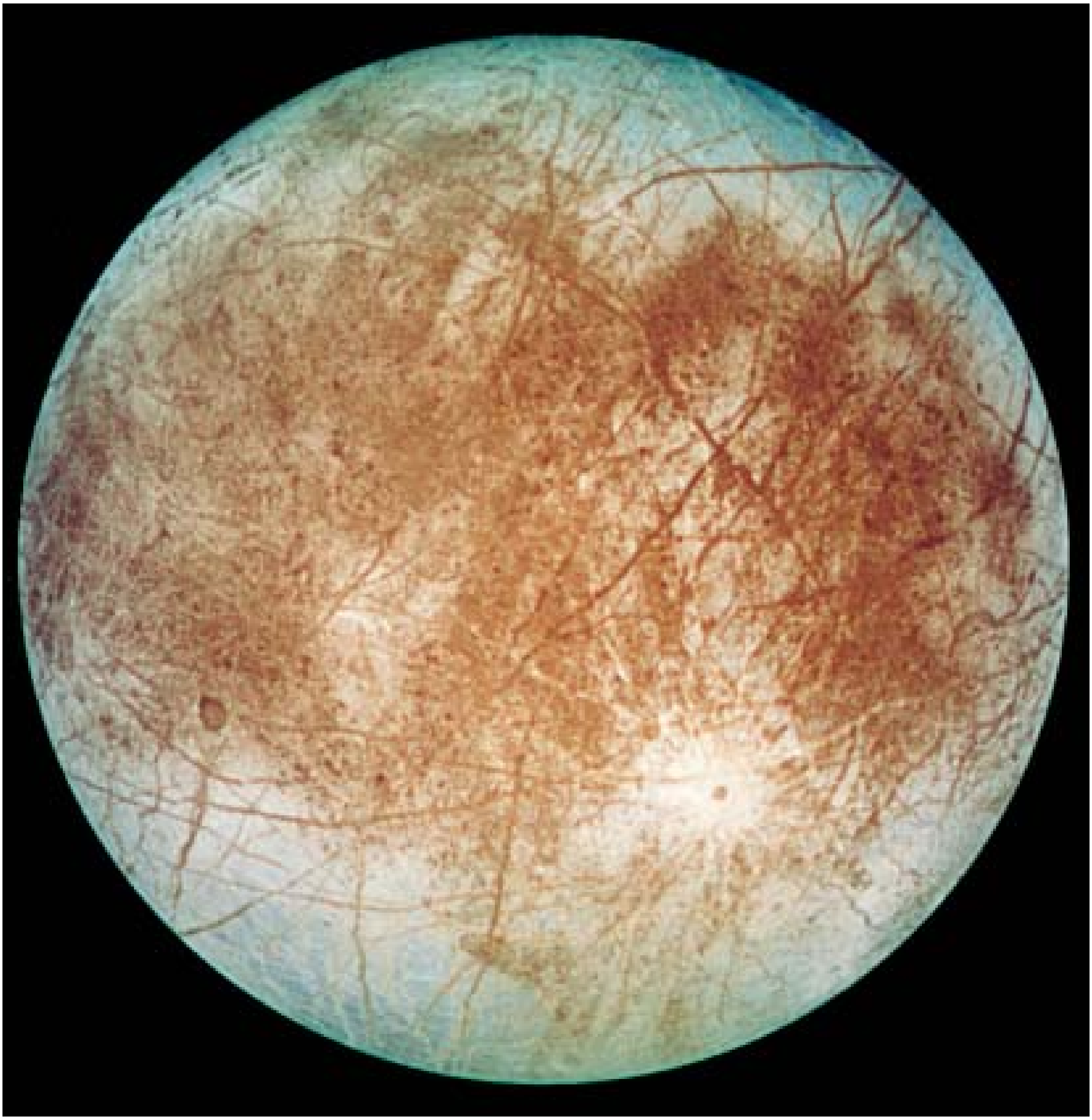

Figure 14.73. Global view of the trailing hemisphere of Europa. This false color image enhances the color differences in the predominantly icy surface. Dark areas are regions of higher concentration of rocky materials derived from the interior or implanted by impact. Bright plains are shown in tones of blue to distinguish possibly coarse-grained ice from fine-grained ice. Long dark lines are fractures in the icy crust possibly produced by tidal stresses. The bright feature containing a central dark spot in the lower third of the image is the impact crater Pwyll (about 50 km in diameter). This image of Europa was taken on 7 September 1996 by the solid-state imaging camera on the Galileo spacecraft.

Figure 14.74. Global image of Ganymede (natural color) obtained by the Galileo spacecraft on 26 June 1996. North is to the top of the picture and the sun illuminates the surface from the right. The dark areas are older, more heavily cratered regions and the lighter areas are younger, tectonically deformed regions. The brownish-gray color is due to mixtures of rocky material, probably derived from impacts, and water ice. Bright spots are geologically recent impact craters.

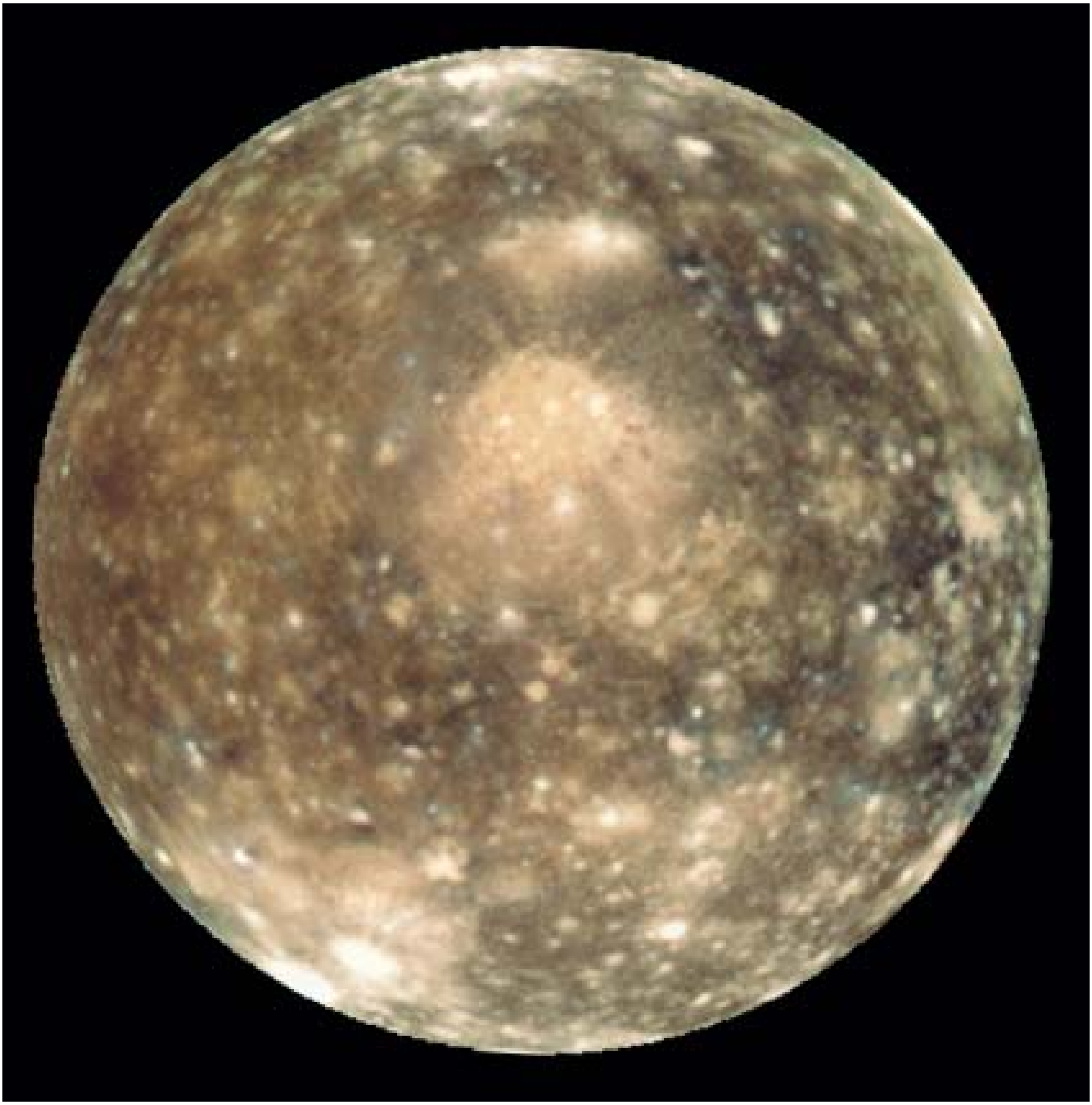

Figure 14.75. Global view of Callisto (false color). The image is centered at 0.5° south latitude and 56.3° longitude. North is to the top of the image and the sun illuminates the surface from near center. The images were taken on 5 November 1997 by the Galileo spacecraft on its 11th orbit of Jupiter. The large bright feature near the center is the ancient, multi-ring impact structure Valhalla, about 600 km in diameter and surrounded by concentric rings 3,000–4,000 km in diameter. The surface is predominantly ice with admixtures of rocky material from impacts. Brighter regions are areas of cleaner ice possibly exposed by impact excavation.

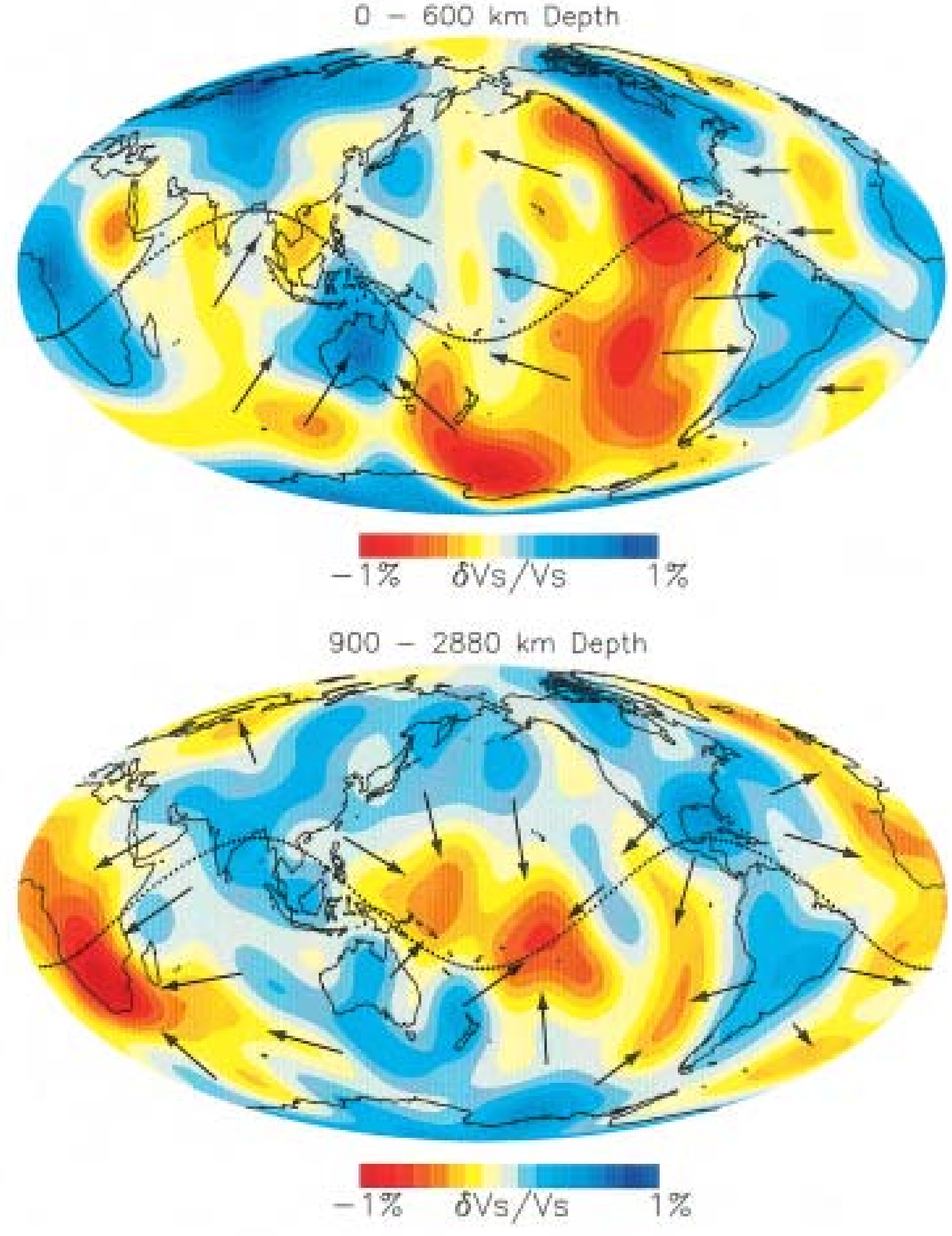

Figure 15.1. The pattern of large-scale mantle heterogeneity with the possible pattern of mantle convection. Top panel: Contours of seismic shear wave heterogeneity from Li and Romanowicz (1996) averaged over the upper mantle (0–600 km depth). The arrows indicate the direction and relative magnitude of horizontal transport in the upper mantle, inferred from the direction of plate motions and the pattern of seismic heterogeneity. Bottom panel: Contours of heterogeneity from the same seismic tomography model, averaged over the lower mantle (900–2,880 km depth). The arrows indicate the direction of horizontal transport in the lower mantle, assuming the seismic heterogeneity is proportional to density heterogeneity. The dotted curve indicates the cross-section shown in Figure 15.2.

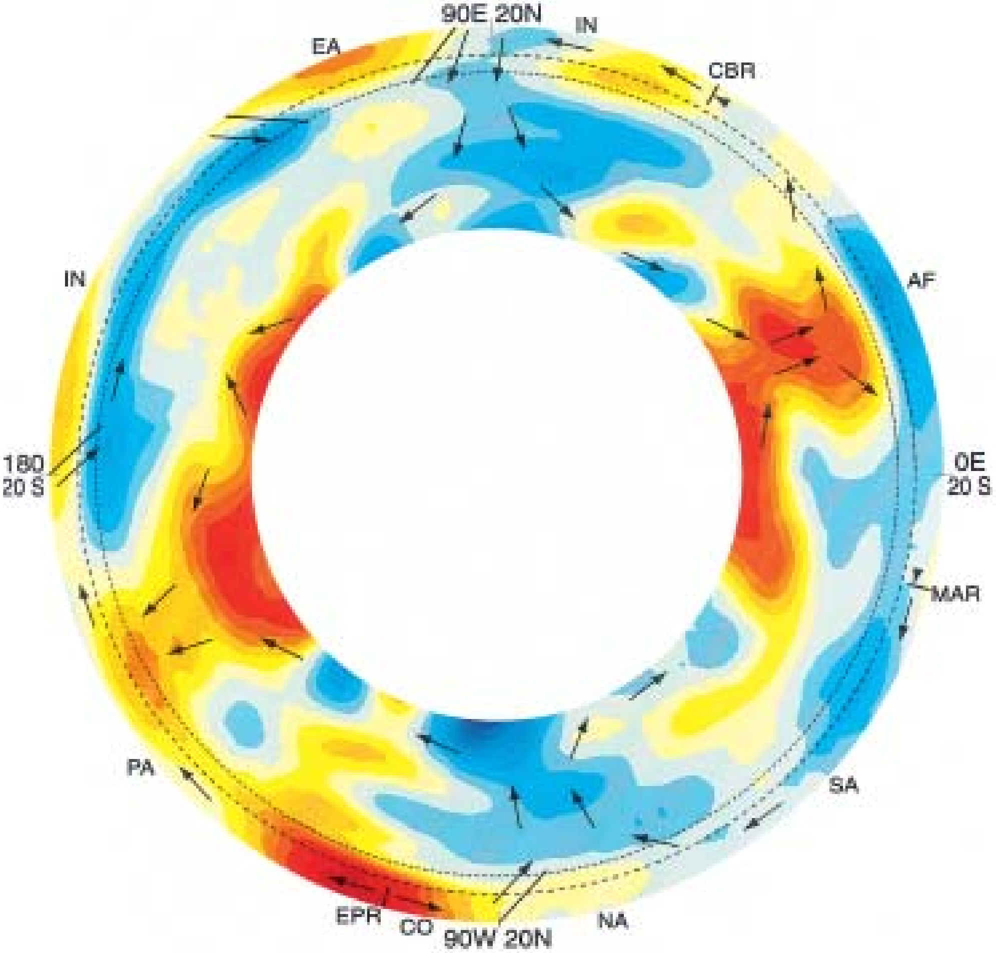

Figure 15.2. Cross-section of the Li and Romanowicz (1996) seismic tomography model along the slice shown in Figure 15.1. Color contours are the same as in Figure 15.1. The 410 and 660 km seismic discontinuities are shown as long and short dashed lines, respectively. The latitude of the slice θ varies with longitude ϕ as $\theta_0 \cos(2\phi)$ with θ_0 corresponding to -20°. The slice latitude is 20°N at longitudes 90°E and 90°W, and is 20°W at longitudes 0° and 180°, at the locations indicated on the diagram. This slice intersects the major seismic anomalies in the lower mantle and is oblique to the direction of plate motions. The plates, spreading centers, and subduction zones along the slice are shown for reference. Subduction zones are indicated by dipping line segments. Plate motion at spreading centers is indicated by double arrows, with direction of ridge migration indicated by parallel arrows. EPR = East Pacific Rise; MAR = Mid-Atlantic Ridge; CBR = Carlsburg Ridge. Plates: EA = Eurasian; IN = Indian; PA = Pacific; NA = North American; SA = South American; AF = African; CO = Cocos. The arrows indicate the pattern of large-scale flow assuming whole mantle convection, with the seismic heterogeneity proportional to density heterogeneity